The Effects of Crystal Lattice Distortion on Trace Element Mobility and U-Pb Isotope Systematics in Zircon: Examples from the Lewisian Gneiss Complex, Northwest Scotland

John M. MacDonald[1], John Wheeler[1], Simon L. Harley[2], Elisabetta Mariani[1], Kathryn M. Goodenough[3], Quentin Crowley[4], Daniel Tatham[1]

[1] School of Environmental Sciences, Jane Herdman Laboratories, University of Liverpool, L69 3GP, UK

[2] School of GeoSciences, Grant Institute, The King's Buildings, West Mains Road, Edinburgh, EH9 3JW, UK

[3] British Geological Survey, Murchison House, West Mains Road, Edinburgh, EH9 3LA, UK

[4] Dept. Geology, School of Natural Sciences, Trinity College, Dublin 2, Ireland, IE

Corresponding author: John M. MacDonald

Postal: School of Environmental Sciences, University of Liverpool, L69 3GP, UK.

Email: jmacd@liv.ac.uk

Telephone: 01517945201

Abstract Zircon is a key mineral in geochemical and geochronological studies in a range of geological settings as it is mechanically and chemically robust. However, distortion of its crystal lattice can change the abundance and distribution of key elements such as U and Pb. Our Electron Backscatter Diffraction (EBSD) analysis of ninety-nine zircons from the Lewisian Gneiss Complex (LGC) of northwest Scotland has revealed five zircons with lattice distortion. The distortion can take the form of gradual bending of the lattice or division of the crystal into subgrains. Weighted Burgers Vectors analysis of EBSD data lends support to the observation that the zircon lattices have been distorted either by post-crystallisation plastic distortion or as a growth microstructure. Three of the five distorted zircons, along with many of the undistorted zircons in the population, were analysed by ion microprobe to measure U and Pb isotopes, Ti and REEs. Comparison of Th/U ratio, U-Pb age, REE pattern and concentration, and Ti abundance between zircons with and without lattice distortion indicates that the distortion

heterogeneously affects these elements and isotopes within single crystals, within samples and between localities. Th/U ratios in distorted zircons ranges from 0.3-3.2 while REE patterns vary heterogeneously, sometimes depleted in heavy REEs or lacking a Eu anomaly. Ti-thermometry records temperatures that were either low (~700°C) or (~900°C) high relative to undistorted zircons. One distorted zircon records concordant U-Pb isotopic ages of 2420-2450Ma but this does not correlate with any previously dated tectonothermal event in the LGC. Two other distorted zircons give discordant ages of 2331Ma and 2266Ma, defining a discordia lower intercept within error of a late amphibolite-facies tectonothermal event. This illustrates that Pb may be mobilised in distorted zircons at lower metamorphic grade than in undistorted zircons. These findings show the advantages in testing for lattice distortion by EBSD prior to micro-beam analysis so as to avoid making oversimplified geological interpretations based on such grains, and also that distorted lattices record information on otherwise cryptic events.

Keywords – zircon, lattice distortion, trace elements & isotopes, EBSD

Introduction

Zircon is a common accessory mineral in a wide range of sedimentary, igneous and metamorphic rocks. It has a high volume diffusion closure temperature for radiogenic Pb (Cherniak and Watson, 2003) and is regarded as a mechanically and chemically robust mineral (Finch and Hanchar, 2003) which is suitable for geochemical investigation of Precambrian geological events. The incorporation of uranium but not lead makes it ideal for radiometric dating; it also contains other elements such as hafnium, titanium and the Rare Earth Elements (REE) which allow a range of geological interpretations to be made.

Populations of zircons are routinely analysed to determine the tectonothermal evolution of rocks throughout the world, generally involving U-Pb isotope and trace element measurements. Recent research, however, has indicated that some of this isotopic and trace element analysis could be compromised by plastic deformation of the zircon crystal lattice (Reddy et al., 2006; Timms et al., 2006a; Timms et al., 2006b; Timms et al., 2011). Plastic deformation occurs when forces applied to a grain cause the crystal lattice to bend and distort through movement of lattice dislocations; crystals may also grow with defects and therefore have a distorted lattice from the time of

their initial formation. Zircon analysis has conventionally been guided by Backscattered Electron (BSE) and Cathodoluminescence (CL) imaging in a Scanning Electron Microscope. These techniques show up internal crystal zoning and highlight fractures. Fractures are generally avoided in subsequent analysis as they may contain contamination or may have lost or gained key elements, which would result in data giving meaningless geological interpretations. While BSE and CL can show brittle deformation (fracturing) of the crystal lattice, they do not show plastic lattice distortion.

The technique required to reveal lattice distortion is Electron Backscatter Diffraction (EBSD) (Prior et al., 2009). EBSD mapping is conducted inside a Scanning Electron Microscope. The electron beam rasters across the sample surface and at each point a Kikuchi (diffraction) pattern is obtained. EBSD software automatically indexes prominent lattice planes from the diffraction pattern which are controlled by the crystal lattice orientation (Prior et al., 1999). If there is variation in the crystallographic orientation across a crystal (lattice distortion), this will be shown by an EBSD map. Reddy et al. (2006) first showed that lattice distortion, in the form of low-angle boundaries from the plastic deformation of zircon, acted as enhanced diffusion pathways for trace elements. CL imaging of a single zircon megacryst from an Indian Ocean gabbro revealed narrow lines of reduced CL emittance, corresponding with the low-angle boundaries revealed by EBSD. Ion microprobe analysis of REEs indicated that in the part of the megacryst which had been plastically deformed, REE abundance had been modified from that in the undeformed part; REE patterns showed a relative enrichment in middle REEs and depletion in heavy REEs. Timms et al. (2006b) investigated the effects of lattice distortion formed by plastic deformation on the U-Th-Pb system in a zircon megacryst from the Lewisian Gneiss Complex (LGC) of Northwest Scotland (the same host rocks as the zircon population in this study). They found that, as with REEs, low-angle boundaries within the zircon megacryst acted as enhanced diffusion pathways for U and Th; the highest measured concentrations and Th/U ratios were found to be in these microstructures. U-Pb ages were uniform across the megacryst which led the authors to infer that plastic deformation had occurred shortly after crystallisation. Timms et al. (2011) examined another zircon megacryst, this time from a Siberian xenolith. As with the zircons from the LGC and Indian Ocean, this megacryst contained subgrains separated by low-angle boundaries. They determined that Ti is also affected by lattice distortion, as with REE and U-Th-Pb in their previous studies. The low-angle boundaries were depleted in Ti relative

to the subgrains and this could not be explained by volume diffusion alone – the low-angle boundaries were acting as fast diffusion pathways.

The previous work documented examples of plastic deformation in single zircon megacrysts; in this contribution we investigate the frequency, effects and causes of plastic deformation across a large population of zircons of more normal size (<200μm length) of the type routinely used for U-Pb dating and other geochemical analysis. Our multigrain study comprises fifty-five in-situ zircons and forty-four grain-mounted zircons, all of which we have analysed by EBSD; a subset of zircons with and without lattice distortion were analysed by ion microprobe for U-Pb, REE and Ti and we document the effect of the lattice distortion on the mobility of these elements and isotopes. These were chosen based on whether they were large enough for subsequent ion microprobe analysis to measure the effects of lattice distortion. Our aim is to understand the frequency, effects and causes of lattice distortion in a zircon population, in the context of the tectonothermal evolution of the LGC. We highlight the advantages of conducting EBSD analysis prior to ion microprobe analysis – it allows the identification of zircons with lattice distortion which may yield different trace element and isotope data to undeformed zircons and therefore record different aspects of the formation and tectonothermal evolution of their host rocks.

Geological Setting

Rocks from the Lewisian Gneiss Complex (LGC) of northwest Scotland were chosen for this study. The LGC outcrops along the coastal strip of the northwest mainland as well as most of the Outer Hebrides (Fig. 1a). The LGC is composed dominantly of tonalite-trondhjemite-granodiorite (TTG) gneisses with subordinate mafic and metasedimentary units, cross-cut by the mafic Scourie Dyke Swarm and minor granite and pegmatite sheets (e.g. Peach et al., 1907; Tarney and Weaver, 1987). Sutton and Watson (1951) distinguished two tectonothermal events, one before and one after intrusion of the Scourie Dykes; the later of these two events, the Laxfordian, comprised static and dynamic amphibolite-facies retrogression and heterogeneous deformation across the LGC. Sutton and Watson named the pre-Scourie dyke event the 'Scourian' but it has since been subdivided into the Badcallian (Park, 1970) and the Inverian (Evans, 1965). Both the Badcallian and Inverian are heterogeneously overprinted by the Laxfordian and are only preserved in certain areas of the complex, most notably the 'Central Region' of Sutton and Watson (1951), the area around Scourie. Field mapping and petrography showed that the

Inverian assemblage is also amphibolite-facies, whilst the earlier Badcallian is granulite-facies.

U-Pb dating of zircon has been widely applied to the LGC. Different workers have recorded a range of ages from different parts of the LGC (e.g. Corfu et al., 1994; Corfu et al., 1998; Whitehouse and Bridgwater, 2001; Kelly et al., 2008; Whitehouse and Kemp, 2010) but it has proved difficult to confidently match zircon ages to the field geology. It has also been suggested that the LGC is composed of discrete terranes based on U-Pb zircon ages (Friend and Kinny, 1995; Kinny and Friend, 1997; Friend and Kinny, 2001; Love et al., 2004; Kinny et al., 2005; Love et al., 2010) but the complex age patterns are difficult to interpret and there remains the problem of linking zircon data to field relationships. Due to the only very recent deployment of the EBSD technique on zircon, it is possible that lattice distortion may have played a role in these complex age patterns and may yield further information not stored in undistorted zircons.

Methodology

Detailed field maps of localities in the LGC were made to provide a field context of deformation conditions at the whole-rock scale and a framework for sampling. Thin and thick sections were cut from samples and zircons were located on these using BSE imaging. Thin sections were polished to 0.25µm grade using progressively finer diamond paste and finally colloidal silica solution. For SIMS analysis, the thin sections were chopped up and the relevant parts were mounted onto a one inch glass round with epoxy resin suitable for the ion microprobe sample holder. Zircons were also mechanically separated from the same samples.

BSE and CL imaging were carried out in a Philips XL30 SEM at the University of Liverpool while EBSD was conducted on a CamScan X500 crystal probe with a thermionic field emission gun, also at University of Liverpool. BSE images were taken at 20kV and a spot size of 5 while CL images were taken at 10kV and a spot size of 7, both in the XL30 SEM. EBSD patterns were collected in the X500 and crystallographic orientation data were automatically indexed using the program Flamenco. Working conditions were: 20kV acceleration voltage, 20nA beam current and 25mm working distance. A raster step size of 0.5-2µm was used; analytical errors on diffraction angles are ~0.5°. EBSD analytical parameters broadly follow that of Mariani et al. (2009) and Bestmann et al. (2006). Data was processed and displayed using CHANNEL 5.03 from HKL software. The Tango module of CHANNEL 5.03 was used to clean up the data by removing misindexed points and interpolating around good data. The

datasets were then displayed as maps in Tango. The maps used here are composites of Band Contrast (the pattern quality of the EBSD data) and Texture Component (a false-colour map of crystallographic orientation relative to a given point). EBSD maps are interpreted qualitatively, and quantitatively using a Burgers Vector analysis, to elucidate possible dislocation types responsible for lattice distortion (Wheeler et al., 2009) – this is the first published use of this method on a mineral.

SIMS analysis of zircon was carried out at the NERC Ion Microprobe Facility, University of Edinburgh. Trace elements were measured using a Cameca ims-4f ion microprobe while U-Pb isotopic measurements were made using a Cameca 1270 ion microprobe. Analytical and correction procedures follow those outlined by Kelly and Harley (2005a) and Kelly et al. (2008). Analytical reproducibility during and between analytical periods was tested using analyses of the 91500, SL1 and Plesovice (Slama et al., 2008) zircon standards and NIST SRM-610 glass standard. U-Pb age plots and calculation were made using the computer program Isoplot 4.11.

Results

Lattice distortion in megacrystic zircon has been shown to affect trace element mobility and isotope systematics which are important for petrogenetic investigation (Reddy et al., 2006; Timms et al., 2006b; Timms et al., 2006a; Timms et al., 2011). We set out to study the frequency, causes and effects of lattice distortion in a large population of zircons of the size (c. 100x50µm) conventionally used in geochronological/geochemical studies. Twenty-one samples of tonalitic gneisses and two samples of metasemipelites were collected from localities around the village of Scourie (Fig. 1b). These samples were chosen as they recorded a range of different tectonothermal histories: some preserved early Badcallian or Inverian assemblages and structures while others were pervasively altered in the Laxfordian. From these samples, a population of fifty-five in-situ zircons and forty-four grain-mounted zircons were analysed by EBSD to test for lattice distortion. Some zircons contained fractures which were visible in BSE while most zircons in the population exhibited no lattice distortion; examples of zircons with no lattice distortion and zircons with brittle fractures are shown in Fig. 2. EBSD analysis showed that five zircons out of the ninety-nine have lattice distortions of at least 3°. These are described below in the context of their host rocks.

Zircon GG09/Z1 is from sample JM08/GG09, collected at UK Grid Reference NC178410, ~4.5km southeast of Scourie village (Geisgeil, Fig. 1b). At this locality, weakly-banded amphibolite-facies tonalitic gneiss is cut by a

Scourie Dyke which is in turn cut by a Laxfordian shear zone (Fig. 3a). Sample JM08/GG09 is from the pre-dyke banded tonalitic gneiss and is composed of ~40% hornblende aggregates, ~30% plagioclase, ~30% quartz and occasional biotite and opaques; there are no mineral shape fabrics in this rock (Fig. 4). It is interpreted to be a Badcallian granulite-facies gneiss that was subsequently pervasively statically retrogressed. Zircon GG09/Z1 (Fig. 5a) is a large and unusually squarish-shaped crystal, approximately 200x200µm in size; the lattice distortion is confined to one corner of the crystal, where the lattice gradually bends through 6° out to the tip. BSE imaging (Fig. 5a) shows up a brittle fracture but this is at the opposite end of the crystal to the plastic deformation. The CL pattern for this zircon is fairly irregular – a narrow bright rim partially surrounds a CL-dark zone and fairly uniform lighter zone which appears to have partially overprinted some earlier oscillatory zoning (Fig. 5a). Two narrow darker lines pass through the area of plastic distortion but do not show up on the BSE image and do not appear related to the microstructure (Fig. 5a). This is the only zircon found in this sample. Zircon GG09Z1 was the only zircon found at this locality and so in the absence of undistorted zircons to compare it to, it was not analysed by ion microprobe.

Zircon ST02Z2 is from sample JM09/ST02, collected at UK Grid Reference NC149461, ~1.5km northwest of Scourie village (Sithean Mor, Fig. 1b). At this locality, an enclave of metasemipelite is surrounded by tonalitic gneiss; the field relationships suggest the fabric in the metasemipelite may be pre-dyke (Fig. 3b). Sample JM09/ST02 is from the metasemipelite and is composed of ~30% plagioclase, ~30% quartz aggregates, ~30% biotite laths and relict garnet porphyroblasts. There is a coarse mineral layering and the quartz aggregates define a shape fabric; biotite laths are not aligned and the garnet porphyroblasts are heavily fractured and retrogressed to biotite around the rims (Fig. 4). Zircon ST02Z2 (Fig. 3c) is roughly elliptical and approximately 100µm in length along its long axis; the lattice distortion occurs as a gradual bending from one end of the crystal to the other of around 3° (Fig. 5b). BSE imaging reveals a brittle fracture which correlates to a certain degree with the microstructure shown in the EBSD map but there is still apparent lattice distortion on either side of this (Fig. 5b). The zircon is largely CL-dark with irregular patches of lighter CL response (Fig. 5b).

Zircon BP06ChZ3 is from sample JM09/BP06, collected at UK Grid Reference NC146414, ~3.5km south-southeast of Scourie village (Badcall Point, Fig. 1b). At this locality, an early Badcallian gneissic layering in tonalitic gneiss is cut by a narrow band of possibly Inverian fabric; this is cut by a Laxfordian shear zone which also cuts a

Scourie Dyke (Fig. 3c). Sample JM09/BP06 is from the Laxfordian shear zone and is composed of ~75% sericitised plagioclase, ~20% hornblende and ~5% quartz. Hornblende aggregates define a relatively strong mineral shape fabric (Fig. 4). Zircon BP06ChZ3 (Fig. 5c) is a large irregularly-shaped zircon, approximately 300x150µm in size; lattice distortion occurs in one half of this elongate crystal, up to 10° from the centre to the tip. The stepped nature of the misorientation profile indicates that this crystal is split into subgrains. BSE imaging shows a small fracture along one edge of the crystal which is also picked up by the EBSD but is unrelated to the lattice distortion shown by the EBSD (Fig. 5c). The CL pattern is irregular – it is generally CL-dark with a slightly brighter rim (Fig. 5c). A brighter line passes through the crystal but appears unrelated to the lattice distortion. There are many sinuous CL-dark lines which are sub-parallel to the subgrain walls shown by EBSD; these are similar to features noted by Reddy et al. (2006) and Timms et al. (2011) which they interpret to be subgrain walls. Five ion microprobe analytical spots were made on this zircon (see Fig. 3d), three of which (3, 4 & 5) fell on subgrain walls. For the five spots, Th/U ratios range from 1.7-3.1 while the $^{207}Pb/^{206}Pb$ ages fall between 2422Ma and 2453Ma. The five ages are well within error of each other and are all quite concordant, between -3.02% and +0.26%. Ti concentrations are between 5.7 and 10.7ppm yielding minimum crystallisation temperatures of 694-746°C (Ti-in-zircon geothermometer (Watson et al., 2006)). Four of the five spots show typical zircon REE patterns; zircons are enriched in heavy REEs relative to light REEs but also have a positive Ce anomaly and a negative Eu anomaly (Kelly and Harley, 2005a; Kelly and Harley, 2005b). However, spot 3 has a flat heavy REE pattern with a Lu abundance of only 383ppm. Numerous other zircons were found in this sample, including some located within a few millimetres of zircon BP06ChZ3, but all were undistorted.

Zircons DP02Z2 and DP02Z7 are from sample JM09/DP02, collected at UK Grid Reference NC178359, ~6km west-northwest of Kylesku village (Duartmore Point, Fig. 1b). At this locality, Badcallian granulite-facies tonalitic gneisses are cut by a Scourie Dyke and both are cut by a Laxfordian shear zone (Fig. 3d). Sample JM09/DP02 is from the Laxfordian shear zone and is composed of ~60% hornblende aggregates, ~35% sericitised plagioclase and ~5% quartz. Hornblende aggregates define a strong mineral shape fabric (Fig. 4). Only two zircons were found in this sample which were big enough for ion microprobe analysis and both show lattice distortion. Zircon DP02Z2 (Fig. 5d) is a small elliptical zircon, approximately 80µm in length along its long axis; there is up to 7° misorientation in a band running diagonally across the crystal with one fairly sharp boundary suggesting a fracture, although this

was not seen in BSE imaging. While it does not show any brittle fractures, BSE imaging shows some lines of dark blebs, possibly inclusions (Fig. 5d). Due to the small size of the zircon, it was difficult to get a high-resolution CL image but it shows many sinuous dark lines, as in zircon BP06ChZ3; there is also a bright spot in the centre of the grain which does not correspond with the microstructure (Fig. 5d). Just one ion microprobe analysis was made for this zircon due to its small size. The Th/U ratio is 0.48 while the $^{207}Pb/^{206}Pb$ age of 2331±22Ma is markedly discordant at 6.3%, plotting well below concordia. Light REEs form a typical zircon pattern but there is no Eu anomaly (concentration of Eu is higher than Sm) and the heavy REEs show a flat pattern; the concentration of Lu is only 137ppm. Ti abundance is 21ppm, recording a minimum temperature of 809°C.

Zircon DP02Z7 (Fig. 5e) is a squat, slightly elliptical crystal, approximately 100x80µm in size; there is up to 15° variation in lattice orientation across the crystal, with the most extreme deformation occurring in opposite corners. The EBSD analysis also demonstrates an unusual cross-hatched pattern in lattice orientation in one part of the crystal, with misorientation of up to 7° here (Fig. 5e). BSE imaging shows the core of the grain to have some concentric zoning with fractures emanating from this (Fig. 5e). CL imaging shows the core to be very CL-dark which suggests high U content; the rim, including area of cross-hatched lattice distortion, is CL-bright (Fig. 5e). High U concentrations can induce metamictisation which causes volume increase resulting in the radial fracture pattern (Corfu et al., 2003). While the rim has clearly formed before the metamictisation, it is difficult to say whether the cross-hatched lattice distortion occurred before the metamictisation or is related to it. Just one ion microprobe analysis was made for this zircon due to its small size; the spot was placed in an unfractured part of the CL-bright rim which had the cross-hatched lattice distortion. The Th/U ratio is 0.28 while the $^{207}Pb/^{206}Pb$ age of 2266±40Ma is markedly discordant at 8.5%, plotting well below concordia. The REE pattern is typical of that expected for zircon (Kelly and Harley, 2005a). Ti concentration is 46ppm, recording a minimum temperature of 897°C. No undistorted zircons were found in this sample but sample JM09/DP01, located ~1m away in the marginal part of the shear zone, contained abundant undistorted zircons. Sample JM09/DP01 is composed of ~40% quartz, ~40% plagioclase and ~20% sieve-textured hornblende and quartz, after pyroxene; there is no shape fabric and weak gneissic layering and is therefore much less intensely deformed than sample JM09/DP02. Full ion microprobe data is shown in Supplementary Data Tables 1 & 2; Table 1 summarises the results for each distorted zircon.

Discussion

Comparison of distorted and undistorted zircons

Ion microprobe data from the distorted zircons have been compared to undistorted zircons to illustrate the effects of lattice distortion on trace element mobility and isotope systematics, and the geological conclusions drawn from them. The samples to which the distorted zircons were compared, and the reasons why, are given in Table 2.

U-Th-Pb

As U-Pb zircon dating is a widely used technique, it is important to understand the effects of lattice distortion on U-Th-Pb systematic. As U and Th abundance are linked through radioactive decay but can vary within and between zircons, Th/U ratios are a useful way of comparing distorted and undistorted zircons. Th/U ratios of 1.7-3.1 in zircon BP06ChZ3 were up to three times higher than those of the undistorted comparison zircons from the same sample (generally in the range of 0.7-1.2). Zircons DP02Z2 and DP02Z7 had Th/U ratios of 0.28 and 0.48 respectively which fall within the range of the comparison zircons from sample JM09/DP01 (0.15-1.54) but are lower than the average of 0.63.

In general, the U-Pb ages calculated from distorted zircons were younger than ages from comparison zircons from the same or nearby samples. The five ages from zircon BP06ChZ3 are within error of each other but are younger than the undistorted zircons from that sample (Fig. 6a). Three of the points are very concordant, between +0.5% and -1% concordance, while the other two plot slightly above Concordia (-2% and -3% respectively). This reverse discordance may be explained by the inferred plastic deformation – possibly as a result of U loss through open-system behaviour during bending of the lattice, as found by Timms et al., (2006b). The five ages are slightly younger than previously published ages of 2490Ma for a tectonothermal event in the Central Region/Assynt Terrane (Corfu et al., 1994; Friend and Kinny, 1995). Possible loss of a small amount of Pb from the lattice during plastic deformation would give an age slightly younger than crystallisation; this would suggest that plastic deformation occurred at or after 2490Ma but the precise age of this is uncertain.

Zircons DP02Z2 and DP02Z7 give ages that are younger than all the rest of the analysed zircons in this study, with or without lattice distortion; they are both highly discordant and plot well below concordia, indicating Pb-loss (Fig. 4a). The position and spatial relationship of the ellipses for DP02Z2 and DP02Z7 on a concordia plot line up on a discordia chord with an upper intercept through a cluster of concordant ages at c. 2500 Ma from undistorted zircons from samples JM09/DP01 and JM09/BP06. This discordia has an upper intercept at 2557±36Ma and a lower intercept at 1617±160Ma with a MSWD of 1.13 (Fig. 6b). The age cluster at around 2500Ma is interpreted to be the age of a tectonothermal event – it is the youngest concordant zircon age recorded in the whole dataset and is also close to the 2490Ma tectonothermal event (the Inverian of Corfu et al. (1994) and the Badcallian of Kinny et al. (2005)). Although the lower intercept has a large error, it is within error of published ages for the lower amphibolite-facies Laxfordian tectonothermal event. Kinny and Friend (1997) and Corfu et al. (1994) give U-Pb ages of 1750-1670Ma from rutile and titanite for the Laxfordian. Therefore, these two zircons appear to be recording the Laxfordian event in their U-Pb systematics. An increase in temperature in the Laxfordian may have allowed volume diffusion of Pb out of the zircon and the inherent lattice distortions will have facilitated this. Laxfordian ages are not recorded in any undistorted zircons in this study or in previous studies; this indicates that lattice distortion allows Pb diffusion at lower temperatures than in undistorted zircon, effectively lowering the closure temperature.

Ti Thermometry

Of all the analysed zircons in this study, four of the five spots from zircon BP06ChZ3 had the four lowest Ti concentrations in the whole dataset; the minimum temperatures calculated from this using the Ti-in-zircon geothermometer (Watson et al., 2006) were between 694 and 722°C – well below the main data cluster of 770-810°C in the undistorted zircons from sample JM09/BP06. The undistorted zircons dataset includes one that was located approximately 2mm away from distorted zircon BP06ChZ3, indicating that the distorted zircon has lost Ti from its lattice, most likely during plastic deformation. Zircon DP02Z2 yields a crystallisation temperature of 810°C; this is slightly higher than the highest of the temperatures recorded in undistorted zircons from sample JM09/DP01 but is not strikingly different so lattice distortion is interpreted not to have had any extreme or obvious

296 effects on this particular crystal. In zircon DP02Z7, however, the temperature recorded is 897°C, at least 85° higher
297 than the other analysed zircons. The Ti-in-zircon thermometer used gives true crystallisation temperatures only
298 when buffered by rutile. Rutile is present in most of the samples used in this study but is not in textural equilibrium
299 with the zircon: it forms fine-grained intergrowths with ilmenite indicating that the rutile is replacing the ilmenite
300 (as Luvizotto et al., 2009), likely in the Laxfordian tectonothermal event. As no zircon grew or recrystallised in the
301 Laxfordian, the temperatures are minimum crystallisation temperatures. There are, therefore, two explanations
302 for the relatively high temperature recorded in zircon DP02Z7. The first is that a lack of available Ti in the system
303 (indicated by absence of equilibrated rutile) means that most zircons do not record the ambient temperature
304 through their Ti concentration. Local conditions may allow Ti saturation (and therefore record a more accurate
305 crystallisation temperature) in some zircons such as DP02Z7. The temperature recorded by zircon DP02Z7 is in the
306 range of that calculated by Johnson and White (2011) of 875-975°C from major phase equilibrium modelling in
307 mafic gneisses approximately 10km away from our sample JM09/DP02. However, zircon DP02Z2, located ~8mm
308 from DP02Z7 records a temperature 87° lower; this hypothesis would therefore require a considerable variation
309 over that short distance in Ti availability which seems unlikely. The second explanation is that Ti has moved into
310 the zircon lattice from the matrix along lattice dislocations, perhaps during a thermal event. Impurities in the
311 lattice of a material migrate into lattice dislocations to reduce the stress field around the dislocation (Cottrell and
312 Bilby, 1949) and was found to occur in olivine by Ando et al. (2001) but this concept applies to intracrystal
313 movement. It may be that the grain boundary network was relatively enriched in Ti, perhaps by the breakdown of
314 an adjacent Ti-bearing phase and subgrain walls in the distorted lattice were connected to the grain boundary
315 network. Given that Ti abundance appears to be affected by the presence of lattice dislocations in other zircons,
316 including BP06ChZ3 in this study and the zircon megacryst investigated by Timms et al. (2011), the latter
317 explanation would seem more appropriate.
318
319 *REEs*
320
321 The zircons with no lattice distortion from samples JM09/BP06 and JM09/DP01 show a typical chondrite-
322 normalised zircon REE pattern of increasing abundance from light to heavy REE, with positive Ce anomaly and

negative Eu anomaly (Kelly and Harley, 2005a). Abundances of the different REEs normally vary by less than half an order of magnitude between analytical spots. The data from samples JM09/BP06 and JM09/DP01 were therefore pooled for comparison against the zircons with lattice distortion. Zircon BP06ChZ3 follows the normal pattern but with some deviation and heterogeneity within the crystal: spot 3 has a relatively low concentration of heavy REEs and a slightly flatter heavy REE profile (Yb/Gd = 6.83); all 5 spots are slightly enriched in Pr relative to undistorted zircons; and the Eu anomaly is subdued, with spot 5 actually having more Eu than Sm, the previous element. The Sm/Nd ratio is low – 1.5-2.5 relative to generally 3-4 in undistorted zircons.

The REE abundances of zircon DP02Z7 fall within the range of zircons with no lattice distortion and it has a similar REE pattern but with a subdued Eu anomaly. Zircon DP02Z2 also has a subdued Eu anomaly, with more Eu than Sm. It is strongly depleted in heavy REEs: the concentration of Lu, the heaviest REE, was only 137ppm compared to >700ppm among most comparison zircons; it has a pronounced flat heavy REE pattern, illustrated by a very low Yb/Gd ratio of 3.8. The variations in REE abundances between zircon DP02Z2 and the comparison undistorted zircons shown in Figure 7 are much greater than have been documented previously in distorted zircons.

Cherniak et al. (1997) show that heavy REEs diffuse faster than lighter REEs in an undistorted zircon lattice. Diffusion rates would increase with the fast volume diffusion pathways created by lattice distortion and result in the flattening of the middle-heavy REE pattern. The driver for this heavy REE loss is unclear. A change in partition coefficient due to changing pressure-temperature conditions is unlikely as zircon DP02ZX7, located no more than a centimetre away, does not have the same REE pattern. Re-equilibration with another REE-sequestering phase during metamorphism is also a possible driver but garnet is the main metamorphic mineral that incorporates heavy REEs (Kelly and Harley, 2005b; Kelly et al., 2006) and garnet has not been documented in the TTG gneisses of the LGC.

Nature of the Lattice Distortion

Crystals with lattice distortion may have grown with defects and therefore have had a distorted lattice from the time of their initial formation; alternatively, post-crystallisation plastic deformation may occur when forces applied

to a grain cause the crystal lattice to bend and distort through movement of lattice dislocations. Little is known about zircon deformation so we draw upon the general appearance of microstructures in other minerals to aid our interpretation. We also apply a new method of analysing lattice distortion which gives some information on the Burgers vectors of the geometrically necessary dislocations responsible for distortion (Wheeler et al., 2009). In brief, the "integration" version of this method gives the *net* Burgers vector of all the dislocations passing through any chosen area on an EBSD map. These dislocations may be uniformly distributed, non-uniformly distributed or form subgrain walls. The Weighted Burgers Vector (WBV) is expressed crystallographically, and is best presented normalised to the area of the loop (Fig. 8 and Supplementary Table 3), so it is measured in $(\mu m)^{-2}$ or 10^{12} m^{-2} (we find the former unit more convenient). An example of the meaning of the WBV in Supplementary Table 3 is as follows. Suppose we have a loop of square outline 10 µm x 5 µm, with a WBV of (1, 0, 4) $(\mu m)^{-2}$. This could mean that we have 50 dislocation lines with Burgers vector [100] *and* 200 lines with Burgers vector [001] passing through the square. Or, it could mean we have 50 dislocation lines with Burgers vector [104]. The WBV is an average over the areas of the loop and the types of dislocation threading through that loop – it proves useful, in trigonal, tetragonal and hexagonal phases, for distinguishing Burgers vectors lying in the basal plane from others. In what follows we focus on the *relative* magnitudes of the (symmetrically equivalent) *a* and *b* components, and the *c* component which lies parallel to the 4-fold symmetry axis.

WBV data are overlaid on Texture Component EBSD maps for each of the distorted crystals (Fig. 8). Zircons GG09Z1 and BP06ChZ3 both have lattice distortion patterns suggestive of plastic deformation: the WBV shows variable directions probably due to a mix of dislocations with different Burgers vectors, and there are irregularly shaped subgrain walls. The irregular shapes are indistinguishable from subgrain wall morphologies seen in quartz (e.g. Gleason et al., 1993; Stipp and Tullis, 2003; Heilbronner and Tullis, 2006) and olivine (e.g. Drury, 2005). The distortion of one tip of zircon 9 suggests that particular part of the crystal has been bent, showing that strain uptake in the zircon lattice was heterogeneous in its distribution. In zircon BP06ChZ3, the subgrain structure with parallel subgrain walls also indicates bending of the lattice in a similar fashion. Zircon ST02Z2 may also have had its lattice bent by plastic deformation. In zircon DP02Z2, there is a crude radial pattern of subgrain walls around a slightly misoriented part. This could be a deformation microstructure influenced by the strength heterogeneity caused by the misoriented part, or it is conceivably caused by growth defects. The cross-hatched misorientation

pattern in zircon DP02Z7 is most unusual, with straight parallel subgrain walls, and it is difficult to see how it can be explained by plastic deformation. In addition the WBV measurements are dominated by components lying in the *a* and *b* plane (the basal plane). We speculate that this is a growth microstructure, because we are not aware of any similar deformation microstructures, and the Burgers vectors are anomalous.

Heterogeneous Response of Trace Elements and Isotopes to Lattice Distortion

Reddy et al. (2006), Timms et al. (2006b) and Timms et al. (2011) found that, in general, lattice distortion allowed enhanced volume diffusion along fast pathways such as subgrain walls; this generally led to depletion of trace elements in the zircon. In this study, however, we find that lattice distortion causes heterogeneous behaviour within crystals, within samples and between different localities: trace elements and isotopes are depleted in some analyses but enriched in others. Table 3 summarises the differences in response. It would appear that zircons where the crystal may have grown with lattice distortion (DP02Z2 and DP02Z7) are more amenable to later Pb-loss while Ti is not easily lost and may even be gained. However, the effect of this form of lattice distortion on REEs is in itself heterogeneous as shown by the differences in pattern and abundance between zircons DP02Z2 and DP02Z7. This difference may be due to very local conditions, such as other phases and elements available in the grain boundary network. In zircons where the lattice distortion is caused by plastic deformation, Ti is lost more easily and yet Pb is not while there is variation in REEs even within zircon BP06ChZ3. This variability in chemical response to lattice distortion within grains, within samples and between localities emphasises the advantages of analysing zircon populations with EBSD prior to trace element and isotope analysis.

Context of Plastic Deformation

Three of the five distorted zircons were found in samples from Laxfordian shear zones. These are strongly deformed rocks and it would be reasonable to infer that there is a link between deformation at the whole-rock scale and lattice distortion of the zircons. However, the lattice distortion in zircons DP02Z2 and DP02Z7 does not

appear to be caused by plastic deformation and is therefore unrelated to the shear zone deformation. Zircon BP06ChZ3 is also from a Laxfordian shear zone and does appear to have been distorted by plastic deformation. However, the link to shearing is not clear as there are plenty of undeformed zircons from the same sample while the other two plastically deformed zircons (GG09Z1 and ST02Z2) are from non-shear zone rocks. There is, therefore, no simple link between macro-scale deformation and intracrystalline zircon distortion. Despite this, distorted zircons give useful additional insight to the thermal evolution of the host rocks, whether they are shear zones or not.

Conclusions

Analysis of a range of trace elements and isotopes in a population of zircons from the LGC of northwest Scotland has raised the following key points:

1. Five of ninety-nine zircons analysed were found to have distorted lattices, a small but significant proportion, which suggests that lattice distortion of zircon may be more widespread than realised and contests the commonly held assumption that zircon is mechanically robust.
2. Burgers Vectors analysis suggests that three of the five distorted zircons have undergone post-crystallisation plastic deformation to distort their crystal lattices; the other two have lattice distortion patterns not easily explained by plastic deformation and are instead interpreted to have grown with distorted lattices.
3. There is heterogeneity in chemical response to lattice distortion within grains, within samples and between localities. Zircon BP06ChZ3 has high Th/U ratios and slightly young ages reflecting minor Pb loss, relative to zircons from the same sample with no lattice distortion. There is intracrystal heterogeneity in Ti content but it is generally relatively low while some analytical spots measure flat heavy REE patterns and others no Eu anomaly. Zircons DP02Z2 and DP02Z7 differ from BP06ChZ3 in that Th/U ratios are low and Pb-loss significant. There are differences between zircons DP02Z2 and DP02Z7, however: DP02Z7 has a significantly higher Ti content while DP02Z2 has a flat heavy REE pattern. The flat heavy REE pattern is due to the faster diffusion of the smaller heavy REE ions than their larger light and middle REE neighbours,

although the driver for the heavy REE loss is unclear. The variations in REE abundances between zircon DP02Z2 and the comparison undistorted zircons are much greater than have been documented previously in distorted zircons. These heterogeneous effects are summarised in Table 3.

4. Discordant ages of 2331Ma and 2266Ma from two distorted zircons define a discordia lower intercept within error of the previously recorded age of the lower-amphibolite-facies Laxfordian tectonothermal event. Undistorted zircons do not record Laxfordian ages. This suggests that lattice distortion allows Pb diffusion at lower temperatures than in undistorted zircon.

Overall, these findings illustrate the significant and heterogeneous effects of crystal lattice distortion on trace element mobility and isotope systematics in zircon. It highlights the advantages of conducting EBSD analysis prior to ion microprobe analysis to determine if any zircons in the target population have distorted lattices. Rather than discarding such zircons, they may record information about the thermal evolution of the host rocks not otherwise recorded in undistorted zircons.

Figure Captions

Fig. 1 Location maps: **a** Outline map of NW Scotland, shaded areas denote LGC outcrop and dotted box denotes location of map b; location in UK in inset; **b** Map of Scourie area showing the location and geological context of the field localities

Fig. 2 BSE images, lattice misorientation maps and misorientation profiles of examples of zircons without lattice distortion (**a**) and zircons with fractures (**b**)

Fig. 3 Maps of field areas from which analysed zircons were obtained; **a** Geisgeil; **b** Sithean Mor; **c** Badcall Point; **d** Duartmore Point

Fig. 4 Petrographic context of the distorted zircons: plane-polarised light photomicrographs of each sample containing a distorted zircon; Hbl = hornblende, Plag = plagioclase, Qtz = quartz, Grt = garnet, Bt = biotite, Opq = opaque iron oxide

Fig. 5 BSE images, CL images, lattice misorientation maps and misorientation profiles of the five zircons with lattice

457 distortion. The lattice misorientation maps were generated using the "Texture Component" function in the
458 "Tango" module of Channel5 software and illustrate crystallographic orientation relative to a given point. The
459 misorientation profiles show this relative change along a transect. The location of the misorientation profiles are
460 shown by the lines on the associated lattice misorientation maps. Ellipses denote ion microprobe analytical spot
461 locations; on zircon BP06ChZ3, numbers denote spot numbers referred to in the text. **a** GG09Z1; **b** ST02Z2; **c**
462 BP06ChZ3; **d** DP02Z2; **e** DP02Z7

463 **Fig. 6** Wetherill concordia plots; **a** The age relationship of distorted zircons BP06ChZ3, DP02Z2 and DP02Z7 and
464 undistorted comparison zircons from samples JM09/DP01 and JM09/BP06; **b** Concordia plot showing a discordia
465 chord through the ellipses for DP02Z2 and DP02Z7 which has a lower intercept within error of the age of the
466 Laxfordian tectonothermal event.

467 **Fig. 7** Matsuda diagram showing Rare Earth Element patterns and concentrations. Shaded area denotes analyses of
468 undistorted comparison zircons, solid lines denote distorted zircons. Values are normalised against chondrite
469 (McDonough and Sun, 1995).

470 **Fig. 8** Lattice distortion maps (as in Fig. 3) together with the WBV for some example rectangular subareas. The
471 three numbers listed are the *a*, *b* and *c* components of the WBV, measured in $(\square m)^{-2}$.

472

473 **Table Captions**

474

475 **Table 1** Summary table of data for each zircon with lattice distortion

476 **Table 2** Samples from which undistorted zircons have been used for comparison with distorted zircons and the
477 justification for sample choice

478 **Table 3** Summary table of the general and heterogeneous effects of zircon lattice distortion on trace elements and
479 isotopes from Badcall Point and Duartmore Point

480

481 **Acknowledgements**

482

483 This work was carried out under UK Natural Environment Research Council DTG NE/G523855/1 and British

Geological Survey CASE Studentship 2K08E010 to JMM. Carmel Pinnington and Eddie Dempsey are thanked for assistance with SEM analysis. Ion microprobe analysis at the Edinburgh Ion Microprobe Facility was carried out with funding from NERC grant IMF384/1109; Richard Hinton, Cees-Jan De Hoog and John Craven are thanked for ion microprobe support and Mike Hall for assistance with sample preparation. KMG publishes with the permission of the Executive Director of the Geological Survey.

References

Ando, J. et al., 2001. Striped iron zoning of olivine induced by dislocation creep in deformed peridotites. Nature, 414(6866): 893-895.

Bestmann, M., Prior, D.J., Grasemann, B., 2006. Characterisation of deformation and flow mechanics around porphyroclasts in a calcite marble ultramylonite by means of EBSD analysis. Tectonophysics, 413(3-4): 185-200.

Cherniak, D.J., Hanchar, J.M., Watson, E.B., 1997. Rare-earth diffusion in zircon. Chemical Geology, 134(4): 289-301.

Cherniak, D.J., Watson, E.B., 2003. Diffusion in Zircon. In: Hanchar, J.M., Hoskin, P.W.O. (Eds.), Zircon. Reviews in Mineralogy and Geochemistry.

Corfu, F., Crane, A., Moser, D., Rogers, G., 1998. U-Pb zircon systematics at Gruinard Bay, northwest Scotland: implications for the early orogenic evolution of the Lewisian complex. Contributions to Mineralogy and Petrology, 133.

Corfu, F., Hanchar, J.M., Hoskin, P.W.O., Kinny, P.D., 2003. Atlas of Zircon Textures. In: Hanchar, J.M., Hoskin, P.W.O. (Eds.), Zircon. Reviews in Mineralogy and Geochemistry.

Corfu, F., Heaman, L.M., Rogers, G., 1994. Polymetamorphic Evolution of the Lewisian Complex, Nw Scotland, as Recorded by U-Pb Isotopic Compositions of Zircon, Titanite and Rutile. Contributions to Mineralogy and Petrology, 117(3): 215-228.

Cottrell, A.H., Bilby, B.A., 1949. Dislocation Theory of Yielding and Strain Ageing of Iron Proceedings of the Physical Society. Section A, 62(1).

Drury, M.R., 2005. Dynamic recrystallization and strain softening of olivine aggregates in the laboratory and the lithosphere. Geological Society, London, Special Publications, 243(1): 143-158.

Evans, C.R., 1965. Geochronology of the Lewisian Basement near Lochinver, Sutherland. Nature, 204: 638-641.

Finch, R.J., Hanchar, J., 2003. Structure and Chemistry of Zircon and Zircon-group Minerals. In: Hanchar, J., Hoskin, P.W.O. (Eds.), Zircon. Reviews in Mineralogy and Geochemistry.

Friend, C.R.L., Kinny, P.D., 1995. New Evidence for Protolith Ages of Lewisian Granulites, Northwest Scotland. Geology, 23(11): 1027-1030.

Friend, C.R.L., Kinny, P.D., 2001. A reappraisal of the Lewisian Gneiss Complex: geochronological evidence for its tectonic assembly from disparate terranes in the Proterozoic. Contributions to Mineralogy and Petrology, 142(2): 198-218.

Gleason, G.C., Tullis, J., Heidelbach, F., 1993. The role of dynamic recrystallization in the development of lattice preferred orientations in experimentally deformed quartz aggregates. Journal of Structural Geology, 15(9–10): 1145-1168.

525 Heilbronner, R., Tullis, J., 2006. Evolution of c axis pole figures and grain size during dynamic
526 recrystallization: Results from experimentally sheared quartzite. J. Geophys. Res., 111(B10):
527 B10202.
528 Johnson, T.E., White, R.W., 2011. Phase equilibrium constraints on conditions of granulite-facies
529 metamorphism at Scourie, NW Scotland. Journal of the Geological Society, 168(1): 147-158.
530 Kelly, N.M., Harley, S.L., 2005a. An integrated microtextural and chemical approach to zircon
531 geochronology: refining the Archaean history of the Napier Complex, east Antarctica.
532 Contributions to Mineralogy and Petrology, 149(1): 57-84.
533 Kelly, N.M., Harley, S.L., 2005b. Timing of zircon growth during highgrade metamorphism: Constraints
534 from garnet-zircon REE. Geochimica Et Cosmochimica Acta, 69(10): A22-A22.
535 Kelly, N.M., Harley, S.L., Hinton, R.W., 2006. Zircon-garnet REE distribution: events and processes in high
536 grade terrains. Geochimica Et Cosmochimica Acta, 70(18): A312-A312.
537 Kelly, N.M., Hinton, R.W., Harley, S.L., Appleby, S.K., 2008. New SIMS U-Pb zircon ages from the Langavat
538 Belt, South Harris, NW Scotland: implications for the Lewisian terrane model. Journal of the
539 Geological Society, 165: 967-981.
540 Kinny, P.D., Friend, C.R.L., 1997. U-Pb isotopic evidence for the accretion of different crustal blocks to
541 form the Lewisian Complex of northwest Scotland. Contributions to Mineralogy and Petrology,
542 129.
543 Kinny, P.D., Friend, C.R.L., Love, G.J., 2005. Proposal for a terrane-based nomenclature for the Lewisian
544 Gneiss Complex of NW Scotland. Journal of the Geological Society, 162: 175-186.
545 Love, G.J., Friend, C.R.L., Kinny, P.D., 2010. Palaeoproterozoic terrane assembly in the Lewisian Gneiss
546 Complex on the Scottish mainland, south of Gruinard Bay: SHRIMP U-Pb zircon evidence.
547 Precambrian Research, 183(1): 89-111.
548 Love, G.J., Kinny, P.D., Friend, C.R.L., 2004. Timing of magmatism and metamorphism in the Gruinard
549 Bay area of the Lewisian Gneiss Complex: comparisons with the Assynt Terrane and implications
550 for terrane accretion. Contributions to Mineralogy and Petrology, 146(5): 620-636.
551 Luvizotto, G., Zack, T., Triebold, S., von Eynatten, H., 2009. Rutile occurrence and trace element behavior
552 in medium-grade metasedimentary rocks: example from the Erzgebirge, Germany. Mineralogy
553 and Petrology, 97(3): 233-249.
554 Mariani, E., Mecklenburgh, J., Wheeler, J., Prior, D.J., Heidelbach, F., 2009. Microstructure evolution and
555 recrystallization during creep of MgO single crystals. Acta Materialia, 57(6): 1886-1898.
556 McDonough, W.F., Sun, S.s., 1995. The composition of the Earth. Chemical Geology, 120(3-4): 223-253.
557 Park, R.G., 1970. Observations on Lewisian Chronology. Scottish Journal of Geology, 6(4): 379-399.
558 Peach, B.N., Horne, J., Gunn, W., Clough, C.T., Hinxman, L.W., 1907. The Geological Structure of the
559 Northwest Highlands of Scotland. Memoirs of the Geological Survey. H.M.S.O., London.
560 Prior, D.J. et al., 1999. The application of electron backscatter diffraction and orientation contrast
561 imaging in the SEM to textural problems in rocks. American Mineralogist, 84(11-12): 1741-1759.
562 Prior, D.J., Mariani, E., Wheeler, J., 2009. EBSD in the Earth Sciences: applications, common practice and
563 challenges. In: Schwartz, A.J., Kumar, M., Adams, B.L., Field, D.P. (Eds.), Electron Backscatter
564 Diffraction in Materials Science.
565 Reddy, S.M. et al., 2006. Crystal-plastic deformation of zircon: A defect in the assumption of chemical
566 robustness. Geology, 34(4): 257-260.
567 Slama, J. et al., 2008. Plesovice zircon - A new natural reference material for U-Pb and Hf isotopic
568 microanalysis. Chemical Geology, 249(1-2): 1-35.
569 Stipp, M., Tullis, J., 2003. The recrystallized grain size piezometer for quartz. Geophys. Res. Lett., 30(21):
570 2088.

571 Sutton, J., Watson, J., 1951. The pre-Torridonian metamorphic history of the Loch Torridon and Scourie
572 areas in the North-West Highlands, and its bearing on the chronological classification of the
573 Lewisian. Quarterly Journal of the Geological Society, 106.
574 Tarney, J., Weaver, B.L., 1987. Geochemistry of the Scourian Complex: petrogenesis and tectonic
575 models. In: Park, R.G., Tarney, J. (Eds.), Evolution of the Lewisian and Comparable Precambrian
576 High-Grade Terrains.
577 Timms, N.E., Kinny, P.D., Reddy, S.M., 2006a. Deformation-related modification of U and Th in zircon.
578 Geochimica Et Cosmochimica Acta, 70(18): A651-A651.
579 Timms, N.E., Kinny, P.D., Reddy, S.M., 2006b. Enhanced diffusion of Uranium and Thorium linked to
580 crystal plasticity in zircon. Geochemical Transactions, 7: -.
581 Timms, N.E. et al., 2011. Relationship among titanium, rare earth elements, U-Pb ages and deformation
582 microstructures in zircon: Implications for Ti-in-zircon thermometry. Chemical Geology, 280(1-
583 2): 33-46.
584 Watson, E.B., Wark, D.A., Thomas, J.B., 2006. Crystallization thermometers for zircon and rutile.
585 Contributions to Mineralogy and Petrology, 151(4): 413-433.
586 Wheeler, J. et al., 2009. The weighted Burgers vector: a new quantity for constraining dislocation
587 densities and types using electron backscatter diffraction on 2D sections through crystalline
588 materials. Journal of Microscopy-Oxford, 233(3): 482-494.
589 Whitehouse, M., Kemp, A.I.S., 2010. On the difficulty of assigning crustal residence, magmatic protolith
590 and metamorphic ages to Lewisian granulites: constraints from combined in-situ U-Pb and Lu-Hf
591 isotopes. In: Law, R.D., Butler, R.W.H., Holdsworth, R.E., Krabbendam, M., Strachan, R.A. (Eds.),
592 Continental Tectonics and Mountain Building: The Legacy of Peach and Horne. Special
593 Publications. The Geological Society, London.
594 Whitehouse, M.J., Bridgwater, D., 2001. Geochronological constraints on Paleoproterozoic crustal
595 evolution and regional correlations of the northern Outer Hebridean Lewisian complex,
596 Scotland. Precambrian Research, 105(2-4): 227-245.

597

598

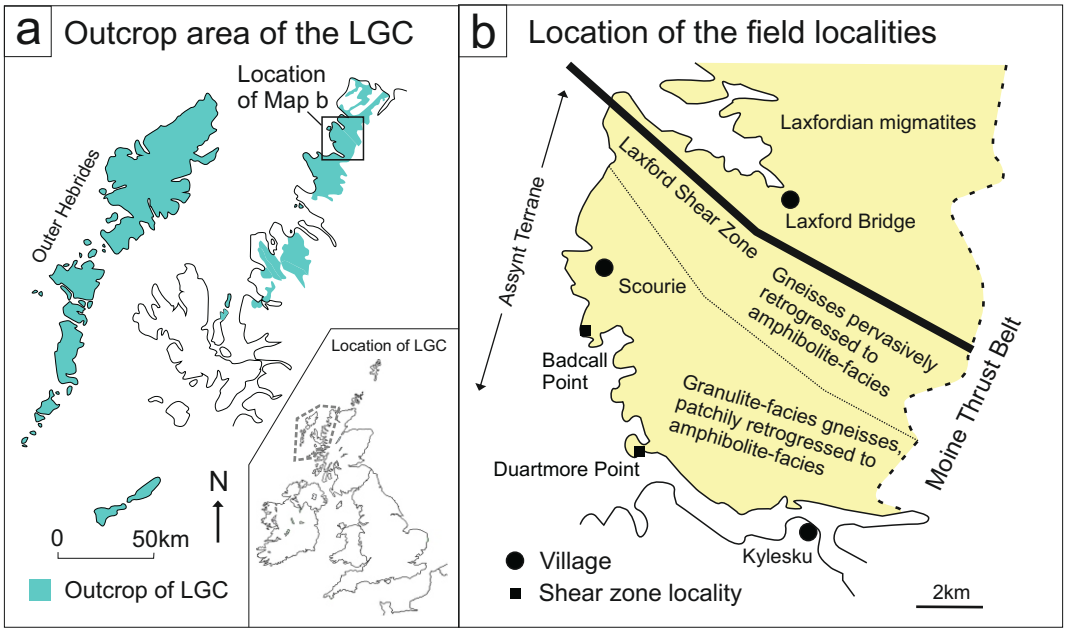
a
Outcrop area of the LGC
Location
of Map b
Outer Hebrides
Location of LGC
N
0
50km
Outcrop of LGC
b
Location of the field localities
Laxfordian migmatites
Laxford Shear Zone
Laxford Bridge
Assynt Terrane
Scourie
Gneisses pervasively
retrogressed to
amphibolite-facies
Badcall
Point
Granulite-facies gneisses,
patchily retrogressed to
amphibolite-facies
Moine Thrust Belt
Duartmore Point
Kylesku
Village
Shear zone locality
2km

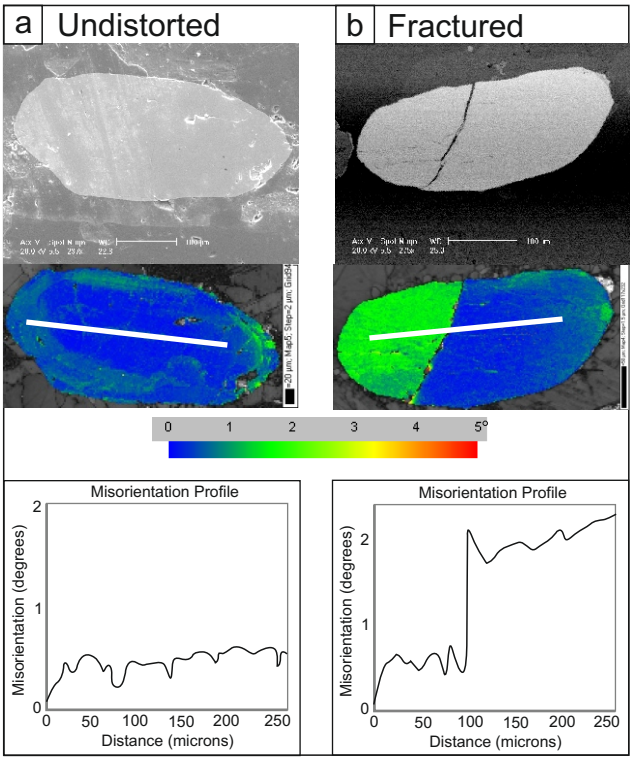
a
Undistorted
b
Fractured
0
1
2
3
4
5°
Misorientation Profile
Misorientation (degrees)
Distance (microns)
0
50
100
150
200
250
1
2
Misorientation Profile
Misorientation (degrees)
Distance (microns)

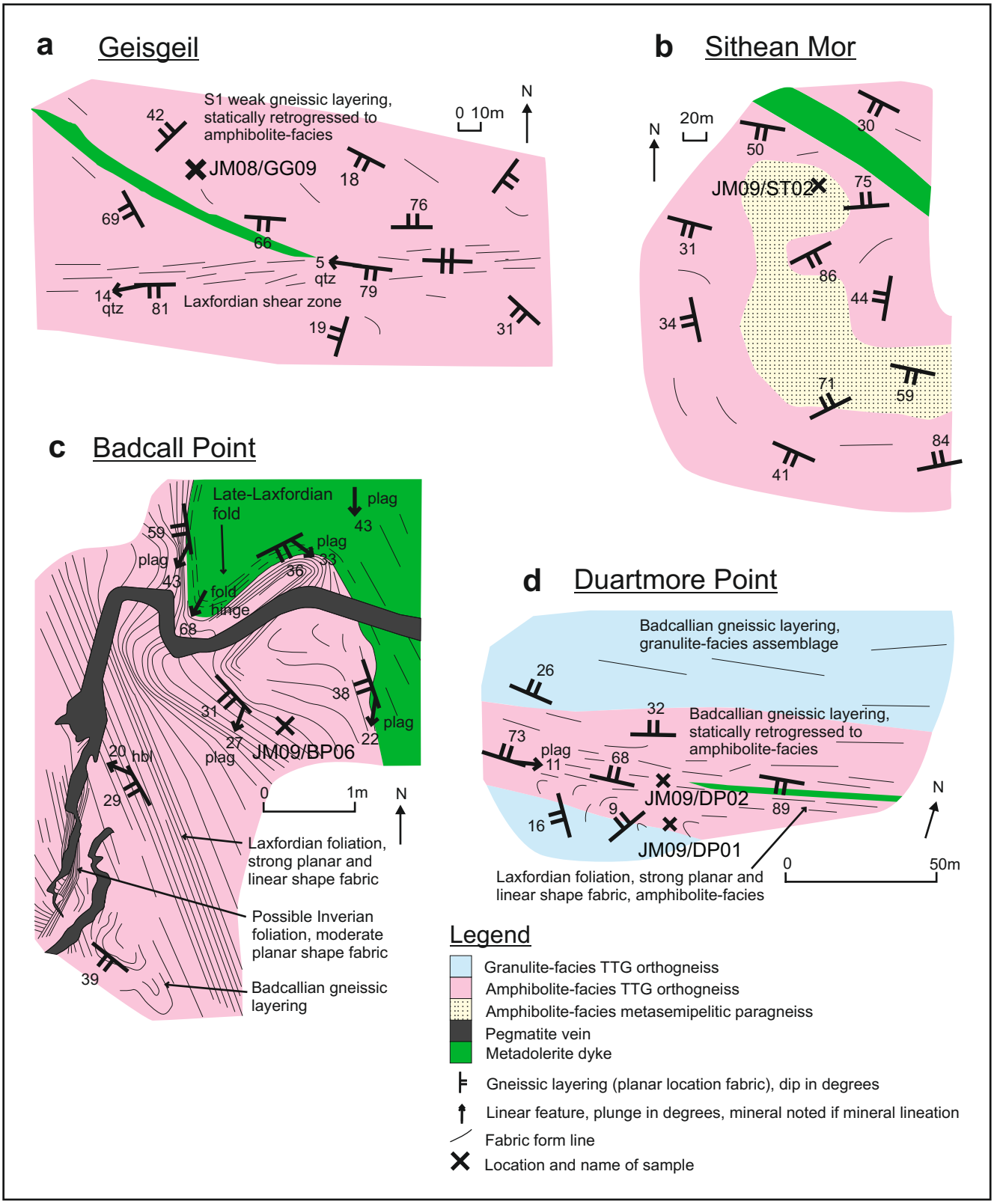
a Geisgeil
S1 weak gneissic layering, statically retrogressed to amphibolite-facies
0 10m
N
42
JM08/GG09
18
69
66
76
5
qtz
14
qtz
81
Laxfordian shear zone
79
19
31
b Sithean Mor
N
20m
50
30
JM09/ST02
75
31
86
44
34
71
59
84
41
c Badcall Point
Late-Laxfordian fold
plag
43
59
plag
43
plag
33
35
fold hinge
68
38
plag
22
31
27
plag
JM09/BP06
20 hbl
29
0
1m
N
Laxfordian foliation, strong planar and linear shape fabric
Possible Inverian foliation, moderate planar shape fabric
39
Badcallian gneissic layering
d Duartmore Point
Badcallian gneissic layering, granulite-facies assemblage
26
32
Badcallian gneissic layering, statically retrogressed to amphibolite-facies
73
plag
11
68
JM09/DP02
89
16
9
JM09/DP01
N
0
50m
Laxfordian foliation, strong planar and linear shape fabric, amphibolite-facies
Legend
Granulite-facies TTG orthogneiss
Amphibolite-facies TTG orthogneiss
Amphibolite-facies metasemipelitic paragneiss
Pegmatite vein
Metadolerite dyke
Gneissic layering (planar location fabric), dip in degrees
Linear feature, plunge in degrees, mineral noted if mineral lineation
Fabric form line
Location and name of sample

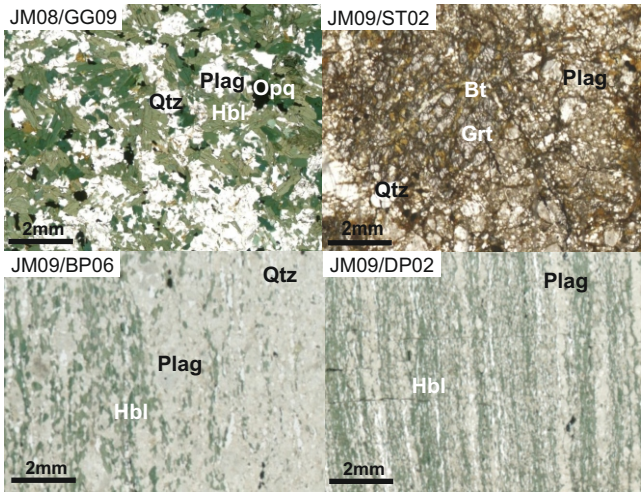
JM08/GG09
Plag
Opq
Qtz
Hbl
2mm
JM09/ST02
Bt
Plag
Grt
Qtz
2mm
JM09/BP06
Qtz
Plag
Hbl
2mm
JM09/DP02
Plag
Hbl
2mm

a: Zircon GG09Z1. Left-right: BSE, CL, Texture Component map, Misorientation Profile

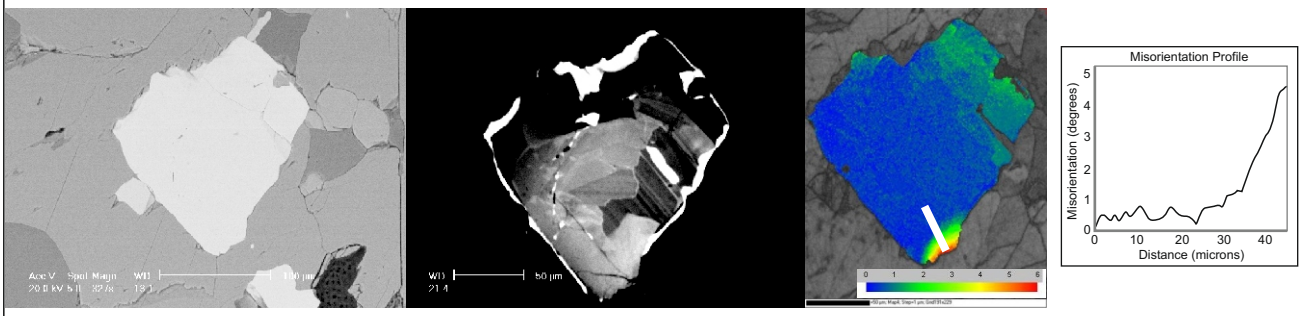

b: Zircon ST02Z2. Left-right: BSE, CL, Texture Component map, Misorientation Profile

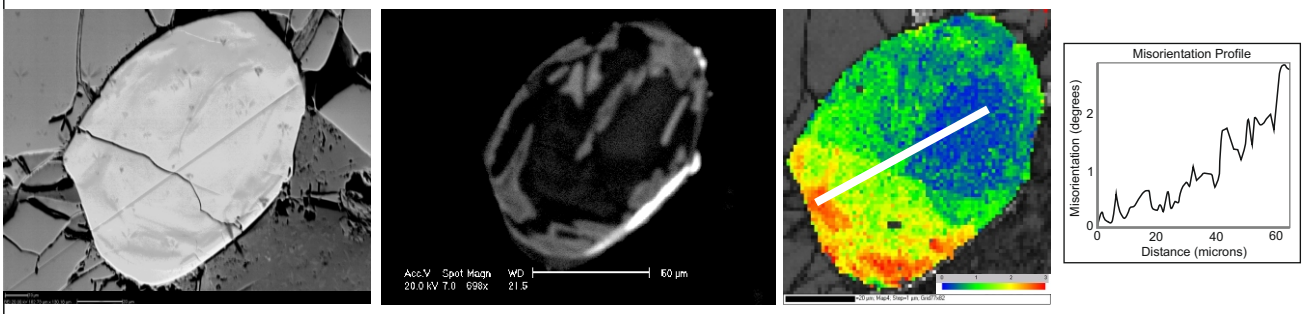

c: Zircon BP06ChZ3. Left-right: BSE, CL, Texture Component map, Misorientation Profile

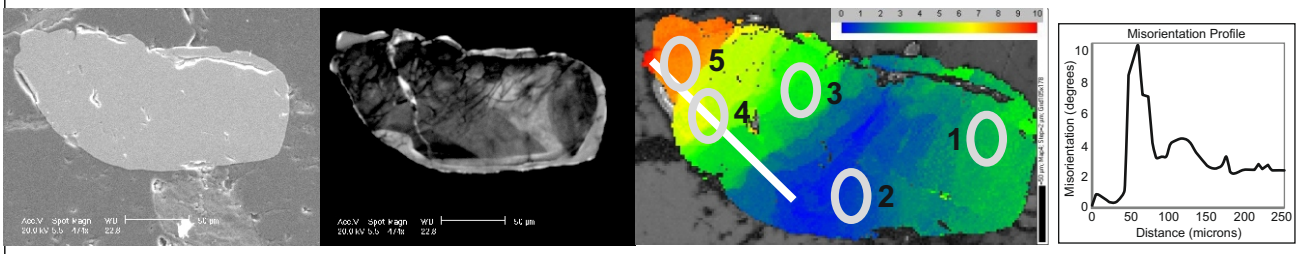

d: Zircon DP02Z2. Left-right: BSE, CL, Texture Component map, Misorientation Profile

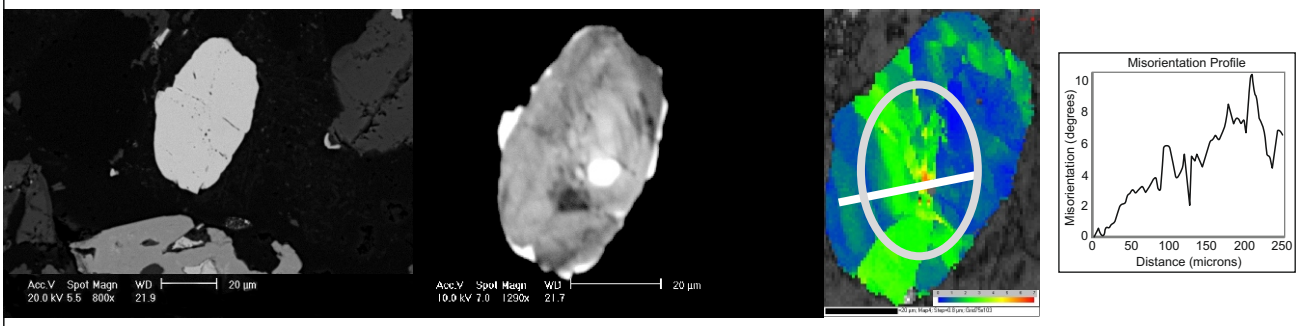

e: Zircon DP02Z7. Left-right: BSE, CL, Texture Component map, Misorientation Profile

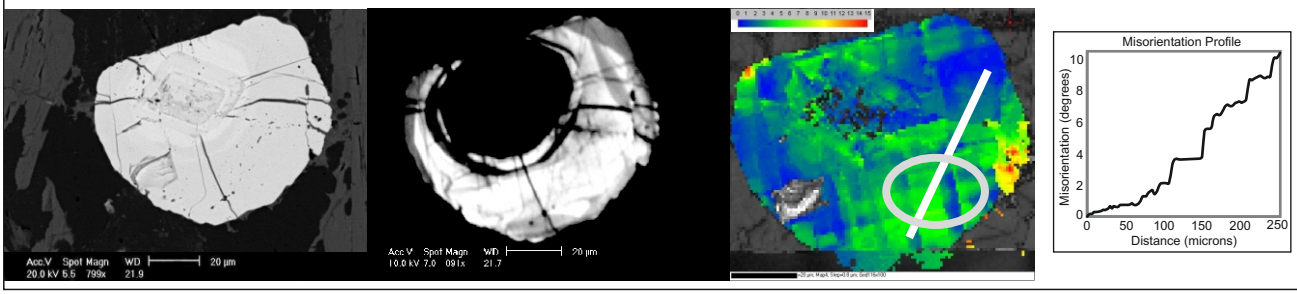

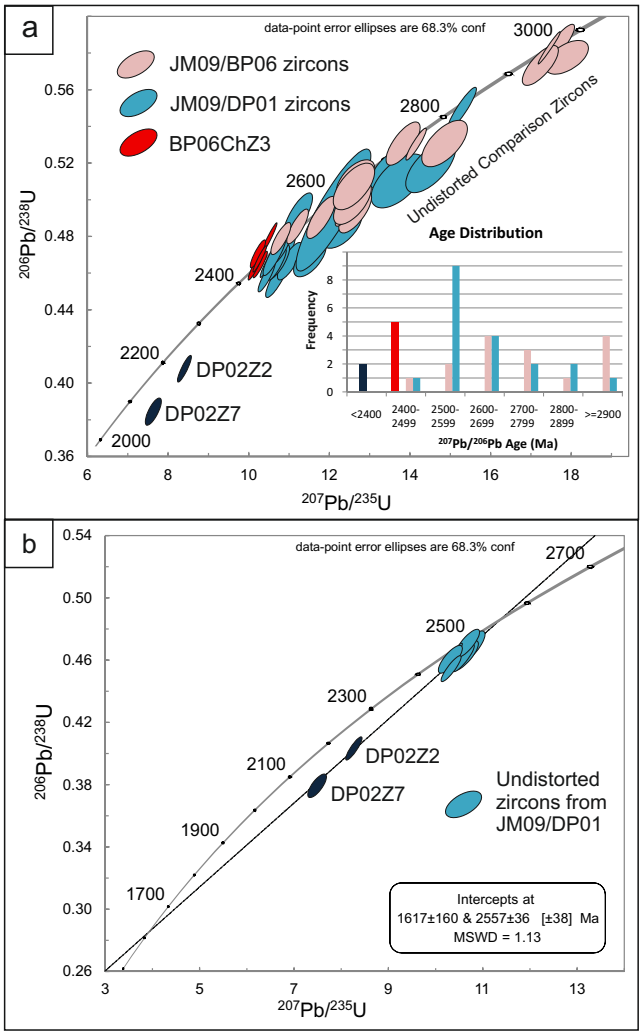
a
data-point error ellipses are 68.3% conf
JM09/BP06 zircons
JM09/DP01 zircons
BP06ChZ3
Undistorted Comparison Zircons
3000
2800
2600
2400
2200
2000
DP02Z2
DP02Z7
Age Distribution
Frequency
<2400
2400-2499
2500-2599
2600-2699
2700-2799
2800-2899
>=2900
207Pb/206Pb Age (Ma)
206Pb/238U
207Pb/235U
0.56
0.52
0.48
0.44
0.40
0.36
6
8
10
12
14
16
18

b
data-point error ellipses are 68.3% conf
2700
2500
2300
2100
1900
1700
DP02Z2
DP02Z7
Undistorted zircons from JM09/DP01
Intercepts at
1617±160 & 2557±36 [±38] Ma
MSWD = 1.13
206Pb/238U
207Pb/235U
0.54
0.50
0.46
0.42
0.38
0.34
0.30
0.26
3
5
7
9
11
13

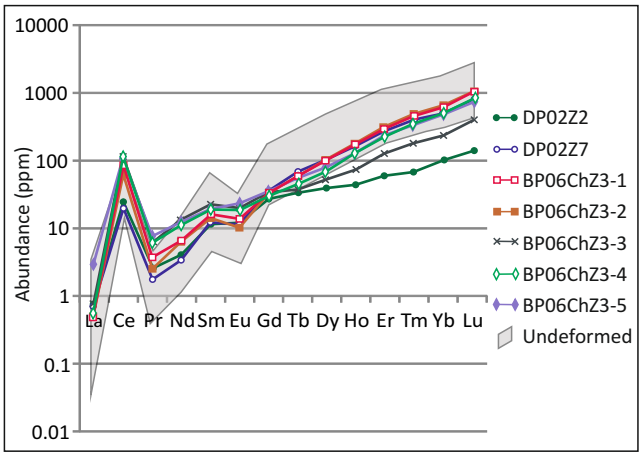
10000
1000
100
10
1
0.1
0.01
Abundance (ppm)
La Ce Pr Nd Sm Eu Gd Tb Dy Ho Er Tm Yb Lu
DP02Z2
DP02Z7
BP06ChZ3-1
BP06ChZ3-2
BP06ChZ3-3
BP06ChZ3-4
BP06ChZ3-5
Undeformed

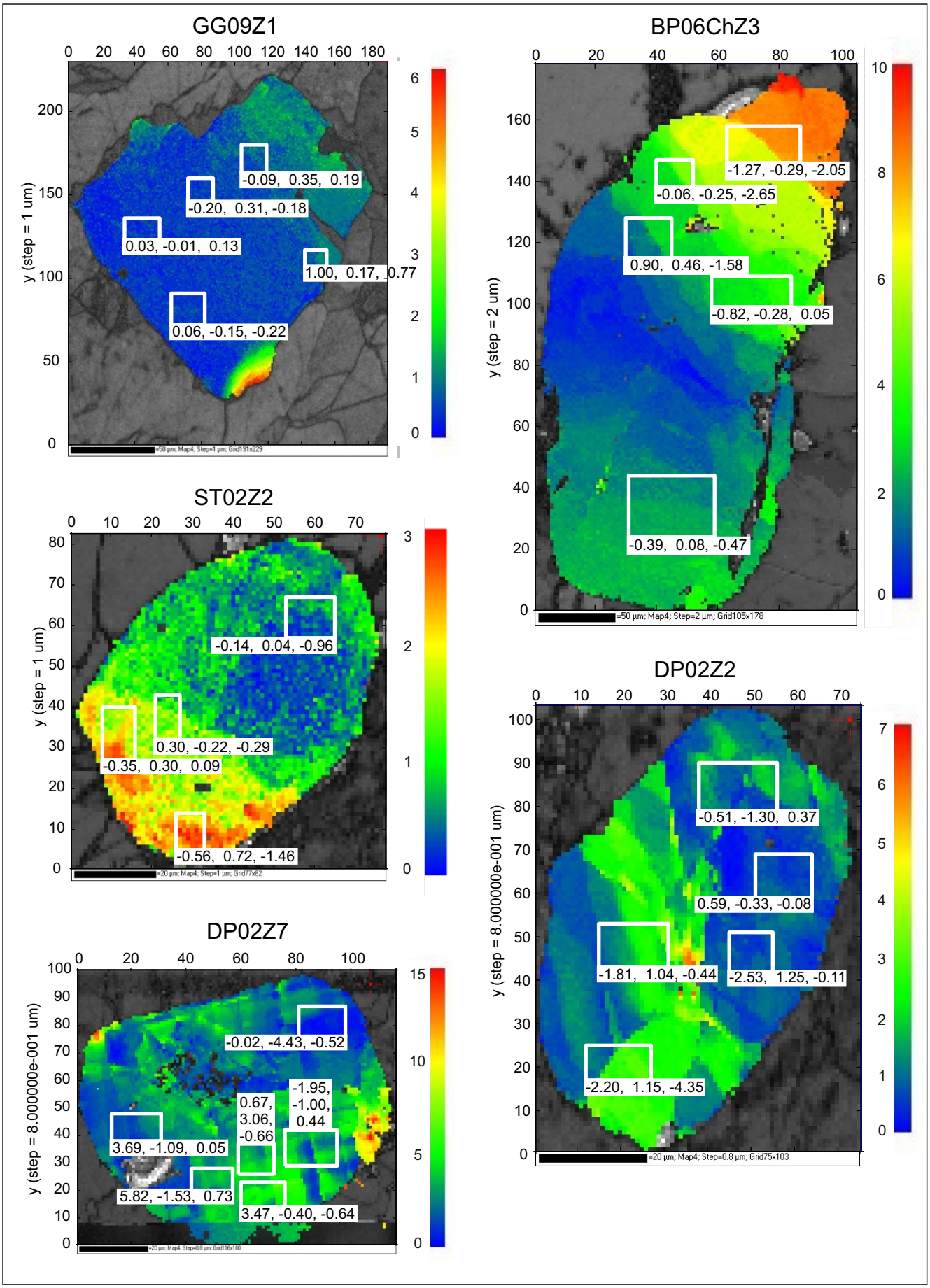
GG09Z1
0 20 40 60 80 100 120 140 160 180
200
150
100
50
0
y (step = 1 um)
-0.09, 0.35, 0.19
-0.20, 0.31, -0.18
0.03, -0.01, 0.13
1.00, 0.17, 0.77
0.06, -0.15, -0.22
6
5
4
3
2
1
0
BP06ChZ3
0 20 40 60 80 100
160
140
120
100
80
60
40
20
0
y (step = 2 um)
-1.27, -0.29, -2.05
-0.06, -0.25, -2.65
0.90, 0.46, -1.58
-0.82, -0.28, 0.05
-0.39, 0.08, -0.47
10
8
6
4
2
0
ST02Z2
0 10 20 30 40 50 60 70
80
70
60
50
40
30
20
10
0
y (step = 1 um)
-0.14, 0.04, -0.96
0.30, -0.22, -0.29
-0.35, 0.30, 0.09
-0.56, 0.72, -1.46
3
2
1
0
DP02Z2
0 10 20 30 40 50 60 70
100
90
80
70
60
50
40
30
20
10
0
y (step = 8.000000e-001 um)
-0.51, -1.30, 0.37
0.59, -0.33, -0.08
-1.81, 1.04, -0.44
-2.53, 1.25, -0.11
-2.20, 1.15, -4.35
7
6
5
4
3
2
1
0
DP02Z7
0 20 40 60 80 100
100
90
80
70
60
50
40
30
20
10
0
y (step = 8.000000e-001 um)
-0.02, -4.43, -0.52
-1.95, -1.00, 0.44
0.67, 3.06, -0.66
3.69, -1.09, 0.05
5.82, -1.53, 0.73
3.47, -0.40, -0.64
15
10
5
0

Zircon	Distortion Pattern	CL	Th/U	$^{207}Pb/^{206}Pb$ Age (Ma)	Ti	REE Pattern
Zircon GG09Z1 from sample JM08/GG09 from Geisgeil	Bending at one corner of the grain	Narrow very bright rim, dark and light zones partially overprinting earlier oscillatory zoning. Two narrow dark lines pass through the area of plastic distortion but do not appear related to the microstructure	-	-	-	-
Zircon ST02Z2 from sample JM09/ST02 from Sithean Mor	Fairly gentle lattice bending across the crystal	Generally quite dark with some irregular lighter patches unrelated to microstructure	-	-	-	-
Zircon BP06ChZ3-1 from sample JM09/BP06 from Badcall Point	Lattice bent in one half of the crystal into a series of subgrains	Generally quite dark with patchy slightly brighter rim, low density of wiggly dark lines	2.824 - much higher than zircons without lattice distortion	2453±16Ma - concordant but slightly younger than youngest ages from zircons without lattice distortion	6.905ppm = 709.44°C - well below the main cluster of temperatures	Low Sm/Nd
Zircon BP06ChZ3-2 from sample JM09/BP06 from Badcall Point	Lattice bent in one half of the crystal into a series of subgrains	As BP06ChZ3-1	1.791 - higher than zircons without lattice distortion	2437±12Ma - concordant but slightly younger than youngest ages from zircons without lattice distortion	5.716ppm = 694.10°C - well below the main cluster of temperatures	Low Sm/Nd
Zircon BP06ChZ3-3 from sample JM09/BP06 from Badcall Point	Lattice bent in one half of the crystal into a series of subgrains	As BP06ChZ3-1 but with a high density of wiggly black lines	3.204 - about 3x higher than zircons without lattice distortion	2437±14Ma - concordant but slightly younger than youngest ages from zircons without lattice distortion	6.187ppm = 700.46°C - well below the main cluster of temperatures	Elevated Pr, low Sm/Nd, flat heavy REE pattern
Zircon BP06ChZ3-4 from sample JM09/BP06 from Badcall Point	Lattice bent in one half of the crystal into a series of subgrains	As BP06ChZ3-1, this spot covers some of the brighter rim	2.716 - much higher than zircons without lattice distortion	2422±20Ma - concordant but slightly younger than youngest ages from zircons without lattice distortion	10.642ppm = 746.47°C - lower than the main cluster of temperatures	No Eu anomaly, elevated Pr, low Sm/Nd
Zircon BP06ChZ3-5 from sample JM09/BP06 from Badcall Point	Lattice bent in one half of the crystal into a series of subgrains	As BP06ChZ3-1 but with a high density of wiggly black lines	2.848 - much higher than zircons without lattice distortion	2440±12Ma - concordant but slightly younger than youngest ages from zircons without lattice distortion	8.103ppm = 722.82°C - well below the main cluster of temperatures	No Eu anomaly, elevated Pr, low Sm/Nd
Zircon DP02Z2 from sample JM09/DP02 from Duartmore Point	Folded pattern across crystal with possibly patchy development of subgrain walls	Medium grey emittance, very bright spot near centre, some irregular dark lines possibly related to microstructure	0.492 - within range of zircons without lattice distortion but below average	2331±22Ma - highly discordant, likely due to Pb-loss during the Laxfordian tectonothermal event, enabled by earlier lattice distortion	20.826ppm = 809.83°C - at the higher end of temperatures recorded by undeformed equivalents	No Eu anomaly, low Sm/Nd, flat heavy REE pattern
Zircon DP02Z7 from sample JM09/DP02 from Duartmore Point	Unusual cross-hatched pattern	Very dark core, very bright rim with dark fracture lines	0.284 - within range of zircons without lattice distortion but well below average	2266±40Ma - highly discordant, likely due to Pb-loss during the Laxfordian tectonothermal event, enabled by earlier lattice distortion	46.557ppm = 896.96°C - at least 85° higher than any other recorded temperatures	No Eu anomaly

	Sample from which undistorted comparison zircons came from			
Distorted Zircon	For U-Pb dating	For Th/U	For REEs	For Ti
BP06ChZ3	**JM09/BP06** – same sample, and **JM09/DP01** – records same age spectrum as **JM09/BP06**	**JM09/BP06** – same sample	**JM09/BP06** – same sample, and **JM09/DP01** – records same compositional range as **JM09/BP06**	**JM09/BP06** – same sample
DP02Z2	**JM09/BP06** – also a Laxfordian shear zone, located only 6km away, interpreted to have underwent same tectonothermal history as **JM09/DP02**, and **JM09/DP01** – records same age spectrum as **JM09/BP06**	**JM09/DP01** – located only one metre from **JM09/DP02** so likely to have similar chemistry	**JM09/DP01** – located only one metre from **JM09/DP02** so likely to have similar chemistry, and **JM09/BP06** – records same compositional range as **JM09/DP01**	**JM09/DP01** – located only one metre from **JM09/DP02** so likely to have similar chemistry
DP02Z7	**JM09/BP06** – also a Laxfordian shear zone, located only 6km away, interpreted to have underwent same tectonothermal history as **JM09/DP02**, and **JM09/DP01** – records same age spectrum as **JM09/BP06**	**JM09/DP01** – located only one metre from **JM09/DP02** so likely to have similar chemistry	**JM09/DP01** – located only one metre from **JM09/DP02** so likely to have similar chemistry, and **JM09/BP06** – records same compositional range as **JM09/DP01**	**JM09/DP01** – located only one metre from **JM09/DP02** so likely to have similar chemistry

Zircons	Distortion	Th/U	$^{207}Pb/^{206}Pb$ Age (Ma)	Ti	REE Pattern
Badcall Point – zircon BP06ChZ3	Plastic Deformation	Relatively high	Concordant but slightly young	Relatively low	Intracrystal heterogeneity in Pr and Eu content and heavy REE pattern and abundance
Duartmore Point – zircons DP02Z2 and DP02Z7	Distortion during crystal growth	Relatively low	Very discordant, young	Variable – average or relatively high	No Eu anomaly, heterogeneity between crystals in Sm/Nd ratio and heavy REE pattern and abundance

Supplementary Data Table 1 Ion microprobe U-Pb data for zircons with and without lattice distortion

Spot	U	Th	Th/U	%c206	207/206	1σ	206/238	1σ	207/235	1σ	207/206 Age	2σ	Disc. (%)
Lattice Distortion													
BP06ChZ3-1	97.1421	267.4700	2.8246	0.3376	0.1598	0.0008	0.4616	0.0049	10.1704	0.1186	2453	16	0.26
BP06ChZ3-2	101.5732	177.3932	1.7916	0.3161	0.1583	0.0005	0.4762	0.0057	10.3929	0.1296	2437	12	-3.02
BP06ChZ3-3	128.3139	400.8327	3.2046	0.1917	0.1583	0.0007	0.4608	0.0052	10.0538	0.1216	2437	14	-0.24
BP06ChZ3-4	114.3285	302.7408	2.7165	0.2264	0.1569	0.0009	0.4676	0.0051	10.1133	0.1261	2422	20	-2.10
BP06ChZ3-5	133.4560	370.5005	2.8480	0.1758	0.1585	0.0006	0.4647	0.0049	10.1591	0.1125	2440	12	-0.84
DP02Z2-2	86.1310	41.3326	0.4923	0.4679	0.1487	0.0010	0.4034	0.0049	8.2714	0.1146	2331	22	6.28
DP02Z7-1	47.0617	13.0373	0.2842	0.6738	0.1432	0.0017	0.3794	0.0050	7.4914	0.1316	2266	40	8.49
Undistorted													
BP06ChZ1-2	421.2984	294.9425	0.7182	0.0000	0.2168	0.0005	0.5826	0.0060	17.4146	0.1824	2956	8	-0.12
BP06ChZ2-1	72.7615	66.1218	0.9322	0.1262	0.2190	0.0016	0.5851	0.0070	17.6676	0.2498	2973	24	0.12
BP06ChZ2-2	78.1524	68.2091	0.8953	4.3550	0.2243	0.0038	0.5773	0.0062	17.8552	0.3564	3011	54	2.43
BP06ChZ2-3	112.4447	109.3900	0.9980	1.0422	0.2177	0.0025	0.5727	0.0074	17.1906	0.2970	2963	38	1.48
BP06ChZ2-9	252.6647	186.0193	0.7553	0.1778	0.1931	0.0009	0.5288	0.0059	14.0787	0.1693	2768	16	1.14
GMBP06Z1-1	22.3329	23.2971	1.0701	3.5087	0.1855	0.0028	0.4908	0.0076	12.5504	0.2703	2702	48	4.74
GMBP06Z1-2	20.4178	20.1850	1.0142	0.2061	0.1817	0.0017	0.4948	0.0078	12.3990	0.2282	2668	32	2.87
GMBP06Z1-3	11.9326	2.7341	0.2351	4.4528	0.1825	0.0035	0.4960	0.0080	12.4824	0.3122	2675	64	2.93
GMBP06Z2-1	24.4032	31.3117	1.3163	0.2677	0.1668	0.0015	0.4829	0.0064	11.1070	0.1799	2526	30	-0.54
GMBP06Z3-1	17.9974	12.4789	0.7113	0.0004	0.1739	0.0022	0.4879	0.0077	11.6991	0.2386	2595	42	1.29
GMBP06Z3-2	21.4970	12.8517	0.6133	0.5550	0.1628	0.0015	0.4761	0.0059	10.6881	0.1646	2485	30	-1.01
GMBP06Z3-3	16.6860	20.7491	1.2757	3.1891	0.1885	0.0026	0.5291	0.0080	13.7498	0.2815	2728	46	-0.36
GMBP06Z4-2	19.3963	20.1803	1.0673	0.3423	0.1790	0.0037	0.5089	0.0074	12.5599	0.3182	2643	68	-0.34
GMBP06Z4-3	19.7820	20.7889	1.0781	0.2551	0.1798	0.0038	0.5052	0.0086	12.5203	0.3418	2650	70	0.53
GMBP06Z6-2	33.9555	39.3851	1.1899	0.1188	0.2027	0.0040	0.5292	0.0086	14.7921	0.3781	2848	64	3.86
DP01Z10-1	13.8737	5.0175	0.3710	0.5374	0.1780	0.0033	0.4651	0.0068	11.4150	0.2679	2634	60	6.53
DP01Z10-2	14.5447	5.0700	0.3576	0.2352	0.1836	0.0042	0.4823	0.0077	12.2085	0.3387	2685	74	5.50
DP01Z4-1	15.2935	2.2430	0.1505	0.0005	0.1665	0.0018	0.4631	0.0063	10.6293	0.1847	2522	36	2.74
DP01Z4-2	14.0372	2.1237	0.1552	0.2163	0.1881	0.0029	0.5144	0.0069	13.3375	0.2705	2725	48	1.82
DP01Z6-1	18.2683	11.0160	0.6186	0.0881	0.1694	0.0016	0.4541	0.0072	10.6051	0.1950	2551	30	5.39
DP01Z6-2	17.1978	8.7872	0.5242	0.1524	0.1663	0.0020	0.4680	0.0072	10.7343	0.2087	2521	38	1.83
DP01Z6-3	57.9532	87.2325	1.5442	0.0254	0.1664	0.0018	0.4601	0.0061	10.5564	0.1797	2521	36	3.21

Supplementary Data Table 1 (cont.) Ion microprobe U-Pb data for zircons with and without lattice distortion

Spot	U	Th	Th/U	%c206	207/206	1σ	206/238	1σ	207/235	1σ	207/206 Age	2σ	Disc. (%)
DP01Z6-4	14.7220	9.5735	0.6671	0.0005	0.1770	0.0026	0.4803	0.0077	11.7252	0.2577	2625	50	3.67
DP01Z6-5	18.5729	8.9376	0.4937	0.3032	0.1708	0.0019	0.4634	0.0069	10.9111	0.2036	2565	36	4.30
GMDP01Z1-1	36.4762	20.7550	0.5837	0.1595	0.1665	0.0011	0.4615	0.0057	10.5964	0.1492	2523	22	3.05
GMDP01Z1-2	27.1502	10.4125	0.3934	0.1859	0.1645	0.0016	0.4709	0.0060	10.6772	0.1704	2502	32	0.59
GMDP01Z2-1	15.0909	11.7015	0.7955	0.0003	0.2251	0.0040	0.6432	0.0116	19.9603	0.5033	3017	56	-6.12
GMDP01Z3-1	15.1231	7.0775	0.4801	0.1965	0.1945	0.0052	0.5082	0.0099	13.6287	0.4489	2780	86	4.71
GMDP01Z4-1	14.8444	7.7706	0.5370	0.4569	0.1637	0.0014	0.4667	0.0074	10.5319	0.1907	2494	28	1.01
GMDP01Z4-2	12.3357	6.6959	0.5568	0.3328	0.1649	0.0022	0.4890	0.0083	11.1158	0.2409	2506	44	-2.41
GMDP01Z6-1	5.4098	3.2021	0.6072	0.8012	0.2029	0.0044	0.5162	0.0096	14.4395	0.4108	2849	70	5.83
GMDP01Z6-3	65.7016	61.0230	0.9528	0.1380	0.2013	0.0013	0.5487	0.0078	15.2286	0.2373	2836	20	0.58
GMDP01Z7-1	14.6709	7.3677	0.5152	0.2841	0.1770	0.0042	0.4920	0.0225	12.0055	0.6184	2624	78	1.71
GMDP01Z8-2	70.9742	72.1669	1.0431	0.1576	0.1648	0.0010	0.4547	0.0055	10.3310	0.1405	2505	20	3.55

Supplementary Data Table 2 Ion microprobe trace element data; element abundances in ppm. Temperatures are calculated using the Ti-in-zircon geothermometer of Watson et al., (2006)

Spot	La	Ce	Pr	Nd	Sm	Eu	Gd	Tb	Dy	Ho	Er	Tm	Yb	Lu	Hf	Sm/Nd	Yb/Gd	Ti	Temp (°C)
Lattice Distortion																			
BP06ChZ3-1	0.509	84.820	3.652	6.556	16.088	13.422	32.613	57.477	101.852	172.214	296.339	448.143	596.920	1002.971	11784	2.45	18.30	6.906	709.44
BP06ChZ3-2	0.546	67.679	2.420	6.259	14.262	9.988	32.849	58.324	103.675	182.414	315.613	490.810	655.528	1025.976	11200	2.28	19.96	5.717	694.1
BP06ChZ3-3	0.828	125.395	5.998	13.316	22.655	20.036	34.069	37.626	52.423	73.445	127.625	180.028	232.783	383.228	8986	1.70	6.83	6.187	700.46
BP06ChZ3-4	0.611	117.496	6.079	11.127	18.817	18.512	29.288	44.022	70.272	129.005	223.038	344.757	486.634	804.472	11233	1.69	16.62	10.642	746.47
BP06ChZ3-5	3.122	116.674	7.815	12.413	19.153	23.160	35.878	53.920	81.130	131.183	234.000	335.413	479.174	708.496	10861	1.54	13.36	8.104	722.82
DP02Z2-2	0.812	24.418	2.546	4.032	11.355	11.915	26.657	33.540	39.291	43.625	59.694	67.206	100.975	136.557	10650	2.82	3.79	20.826	809.83
DP02Z7-1	0.750	22.101	1.680	3.394	12.571	11.258	34.905	67.271	101.659	165.707	268.075	400.101	493.522	772.520	11611	3.70	14.14	46.557	896.96
Undistorted																			
BP06ChZ2-1	0.262	25.208	1.059	2.832	21.870	16.187	92.236	168.875	294.092	476.361	755.791	1011.644	1266.640	1750.057	9423	7.72	13.73	15.841	793.10
BP06ChZ2-2	3.202	22.339	1.736	3.083	14.787	15.244	58.247	108.656	191.756	318.640	530.737	681.450	893.065	1297.193	9315	4.80	15.33	14.533	783.08
BP06ChZ2-3	0.380	31.636	3.981	12.826	57.667	29.237	159.612	263.380	436.641	676.564	1039.902	1337.896	1684.084	2405.919	9147	4.50	10.55	18.165	796.30
BP06ChZ1-2	0.456	46.708	1.570	5.176	20.957	19.174	62.281	104.133	180.110	298.407	515.775	814.130	1177.888	1976.667	10250	4.05	18.91	14.636	775.60
GMBP06Z6-2	0.274	34.024	2.356	5.448	19.877	10.684	66.734	119.479	186.146	319.762	500.244	635.668	820.559	1259.472	13153	3.65	12.30	21.117	811.23
GMBP06Z3-1	0.295	27.062	0.516	1.647	5.150	4.643	41.527	67.155	121.154	179.049	295.394	374.972	464.323	739.675	15697	3.13	11.18	15.385	780.31
GMBP06Z3-3	0.291	26.768	0.522	3.049	8.835	3.431	47.397	92.934	138.163	235.128	315.875	475.506	529.317	767.764	14587	2.90	11.17	16.376	786.26
GMBP06Z1-1	0.473	29.766	1.698	4.344	18.420	9.197	57.687	91.353	148.170	235.437	370.366	497.823	690.087	922.053	8544	4.24	11.96	18.622	798.74
GMBP06Z1-2	0.331	28.587	1.645	2.792	13.861	8.160	40.853	62.458	106.206	159.263	261.566	339.752	444.650	621.454	8244	4.96	10.88	17.870	794.70
GMBP06Z1-3	0.412	23.331	0.597	2.251	8.853	6.158	43.984	68.455	131.691	213.333	323.429	453.441	580.032	786.063	9500	3.93	13.19	15.657	781.97
GMBP06Z4-2	0.322	27.084	1.231	3.034	12.235	7.062	38.429	59.325	97.015	151.286	241.360	335.117	441.839	622.458	8378	4.03	11.50	15.779	782.71
GMBP06Z4-3	0.315	27.126	1.295	3.786	16.507	11.171	49.969	81.792	131.653	206.049	331.160	447.482	548.373	818.360	8457	4.36	10.97	13.777	769.94
BP06ChZ2-9	1.983	69.422	3.621	5.495	19.070	11.539	50.853	83.855	143.450	224.073	363.967	542.828	692.748	1042.069	9214	3.47	13.62	17.577	793.10
GMBP06Z2-1	0.280	39.114	1.840	7.047	20.407	13.057	59.613	97.152	168.089	271.722	385.869	507.895	647.329	1094.593	13145	2.90	10.86	16.718	788.25
GMBP06Z3-2	0.063	24.414	0.868	1.629	10.504	4.910	36.008	56.817	104.805	155.628	270.288	375.008	393.186	697.642	15495	6.45	10.92	14.837	776.88
DP01Z10-1	0.835	32.351	2.105	4.010	15.126	16.795	39.546	62.188	96.931	141.832	219.069	279.753	372.851	540.366	10560	3.77	9.43	20.279	807.17
DP01Z10-2	0.380	25.584	1.354	3.436	13.455	9.750	39.506	59.731	98.317	149.883	221.413	318.818	393.037	565.122	10146	3.92	9.95	19.811	804.85
DP01Z4-1	0.252	35.504	0.985	2.664	15.053	8.674	55.367	94.510	167.354	257.234	424.088	569.555	724.534	1073.943	11351	5.65	13.09	17.782	794.22
DP01Z4-2	0.334	32.356	0.890	2.254	13.182	7.374	48.692	84.172	145.695	232.070	389.025	510.283	626.398	932.480	10869	5.85	12.86	16.386	786.3205
DP01Z6-1	0.577	29.462	1.796	4.099	16.782	12.572	52.518	73.371	117.581	180.907	276.869	364.628	446.311	671.016	9769	4.09	8.50	17.141	790.66
DP01Z6-2	0.348	27.617	1.512	4.111	15.707	12.355	47.428	73.535	114.402	166.527	262.213	363.126	434.981	648.374	10011	3.82	9.17	15.900	783.44

Supplementary Data Table 2 (cont.) Ion microprobe trace element data; element abundances in ppm. Temperatures are calculated using the Ti-in-zircon geothermometer of Watson et al., (2006)

Spot	La	Ce	Pr	Nd	Sm	Eu	Gd	Tb	Dy	Ho	Er	Tm	Yb	Lu	Hf	Sm/Nd	Yb/Gd	Ti	Temp (°C)
DP01Z6-4	0.470	26.429	1.817	3.029	14.733	12.853	40.262	60.385	95.089	142.015	220.156	304.121	376.988	547.683	10119	4.86	9.36	17.784	794.23
DP01Z6-5	0.610	26.933	1.528	4.176	16.488	14.278	48.489	72.465	113.841	171.516	252.744	354.955	452.888	624.431	9240	3.95	9.34	18.594	798.59
GMDP01Z1-1	0.286	27.201	0.784	1.176	7.363	4.663	27.692	50.485	82.041	131.701	222.463	341.822	435.795	690.366	10319	6.26	15.74	13.322	766.83
GMDP01Z1-2	0.211	26.600	0.978	1.595	8.069	7.516	23.064	46.158	83.065	135.103	232.281	340.506	467.335	697.561	10101	5.06	20.26	8.317	725.03
GMDP01Z2-1	0.283	20.940	0.889	2.288	10.756	8.528	32.654	51.127	82.073	120.703	185.969	255.729	339.429	475.447	8234	4.70	10.39	14.944	777.56
GMDP01Z3-1	0.554	24.734	1.739	3.682	14.713	13.208	46.393	78.668	118.386	184.542	288.675	371.668	478.124	714.309	9445	4.00	10.31	20.751	809.47
GMDP01Z4-1	0.237	27.212	1.579	3.694	12.886	10.668	36.154	54.609	87.565	131.555	198.594	270.279	334.199	463.821	8711	3.49	9.24	9.955	740.57
GMDP01Z4-2	0.497	26.106	1.915	3.512	15.310	12.818	42.594	58.424	93.020	139.485	217.206	293.190	378.776	533.577	8120	4.36	8.89	12.779	762.99
GMDP01Z6-1	0.142	24.143	0.721	1.977	9.965	7.383	29.092	49.967	86.043	137.295	218.851	312.171	428.885	599.340	8637	5.04	14.74	13.704	769.45
GMDP01Z6-3	0.293	24.947	0.800	1.877	8.035	8.250	26.386	44.101	71.311	114.170	186.240	272.320	379.406	583.359	9413	4.28	14.38	13.872	770.58
GMDP01Z7-1	0.403	24.979	1.547	3.889	12.366	12.061	40.265	64.756	97.549	148.864	238.019	308.640	391.323	568.659	9538	3.18	9.72	19.312	802.32
GMDP01Z8-2	0.215	24.573	0.728	2.120	11.497	8.743	33.538	59.028	105.167	173.225	280.506	387.490	531.901	846.057	9179	5.42	15.86	15.340	780.03

Supplementary Data Table 3 Weighted Burgers Vector Components

Zircon	WBV components $(\mu m)^{-2}$		
	a	b	c
DP02Z7	5.818451714	-1.530837192	0.7348278
DP02Z7	0.667587253	3.057091938	-0.664922117
DP02Z7	-1.541415728	2.293683425	0.278421873
DP02Z7	3.690870504	-1.091701329	0.052216839
DP02Z7	-1.95445253	-0.996555036	0.439510002
DP02Z7	3.471163111	-0.404811926	-0.640057027
BP06ChZ3	-0.392250754	0.079511301	-0.466440481
BP06ChZ3	0.897371393	0.459410705	-1.579259132
BP06ChZ3	-0.064425821	-0.246092488	-2.650229436
BP06ChZ3	-0.820655344	-0.275542551	0.046607263
BP06ChZ3	-1.272683099	-0.288521403	-2.054086746
ST02Z2	-0.135815398	0.039763594	-0.964733632
ST02Z2	-0.350864785	0.295566389	0.088411989
ST02Z2	-0.564803094	0.718852835	-1.463135911
ST02Z2	0.30138409	-0.216493544	-0.291590971
DP02Z2	0.586971865	-0.326549953	-0.079846346
DP02Z2	-2.52583996	1.249438939	-0.114974262
DP02Z2	-2.203383838	1.154867399	-4.354069848
DP02Z2	-1.814813449	1.038187698	-0.441378318
DP02Z2	-0.507205777	-1.297535881	0.369179538
GG09Z1	0.034882063	-0.01007395	0.131027585
GG09Z1	-0.092853735	0.34571954	0.18788614
GG09Z1	0.995735963	0.170518146	0.771379999
GG09Z1	0.062202565	-0.149489637	-0.21622045
GG09Z1	-0.203296562	0.308071306	-0.177903056